TURBULENCE MODELLING REQUIREMENTS FOR THE PREDICTION OF VISCOUS TRANSONIC AEROFOIL FLOWS

ICAS-92-4.4.2

Leslie J. Johnston

Department of Mechanical Engineering
UMIST, PO Box 88, Manchester M60 1QD, England

Summary

Computational methods for predicting the viscous transonic flow development around aerofoil sections, using the Reynolds-averaged Navier-Stokes equations, require an explicit turbulence model for the Reynolds stresses appearing in the governing mean-flow equations. At present, most existing Navier-Stokes solvers employ eddy-viscosity based turbulence models, generally of simple algebraic type. The range of turbulence modelling options potentially available for use with Navier-Stokes solvers are briefly reviewed in the present paper. These vary in sophistication from the algebraic eddy-viscosity model of Baldwin and Lomax up to full Reynolds-stress closures, which solve modelled transport equations for all the Reynolds stresses. Results are presented using a recently-developed flow solver and employing a one-equation turbulence model, covering a wide range of transonic flow conditions for the Boeing BAC I aerofoil section. The results indicate that reasonably-accurate quantitative predictions of integrated loads, including drag, can be obtained for freestream Mach numbers up to 0.76, at least until the appearance of extensive shock-induced separation. It is concluded, however, that the shock wave/boundary layer interaction is under-predicted, even for fully-attached flow conditions, and that this can be attributed to deficiencies in turbulence modelling at the eddy-viscosity level. A priority research area for the near-future should, therefore, be an evaluation of Reynolds-stress closure models, which should lead to improved physical modelling of the anisotropic development of the Reynolds stresses through the shock wave/boundary layer interaction region.

Introduction

The continuing advances being made in computer speed and memory capabilities are enabling evermore large-scale applications of Computational Fluid Dynamics (CFD) to external aerodynamic flows. Indeed, through the use of block-structured or unstructured computational grid techniques, the aerospace industry is now able to compute the transonic inviscid flow development around complete aircraft configurations. The transonic flow regime is an important area both for the cruise performance of civil transport aircraft and for the manoeuvring of combat aircraft. Inviscid flow analysis methods based on solutions of the Euler equations can provide much useful aerodynamic information for design purposes and, as such, these methods are now displacing older methods based on small-perturbation or potential flow theories. However, despite the high-Reynolds number nature of most external aerodynamic flows, viscous effects are important in many crucial areas. The shock wave/boundary layer interactions present on wings and in jet/afterbody regions at transonic flow conditions are two examples where viscosity plays an important role in the quantitative flow development. Furthermore, the flows of practical interest are generally turbulent in nature, and so the CFD research community is now moving towards the development of computational methods able to predict transonic turbulent flows.

Copyright © 1992 by ICAS and AIAA. All rights reserved.

It is possible, in principle, to compute compressible turbulent flows in a nominally-exact manner using Direct Numerical Simulation (DNS) or Large Eddy Simulation (LES) techniques. The application of DNS or LES to the high-Reynolds number aerodynamic flows of interest to the aerospace industry remains beyond the capability of current supercomputers, however. For this reason, computational methods which employ the Reynolds-averaged Navier-Stokes equations are being actively developed, this being seen as the most practical engineering approach to be taken at the present time. The main problem associated with the Reynolds-averaged Navier-Stokes equations is that they do not form a closed system of equations. The time-averaging procedures used to derive the equations introduce new unknowns, the Reynolds stresses, which must be modelled in terms of known or knowable quantities before solutions can be obtained. Thus, turbulence modelling is becoming increasingly recognised as the most important factor determining the quantitative accuracy of prediction methods solving the Reynolds-averaged Navier-Stokes equations.

The computation of the viscous transonic flow development around two-dimensional aerofoil sections continues to be addressed by many in the CFD research community. This is due to both the intrinsic interest of such flows themselves and also since they provide an efficient means for initial investigation of numerical algorithm and physical flow modelling issues, before recourse needs to be made to expensive three-dimensional computations. The AIAA Viscous Transonic Airfoil Workshop[1] of 1987 provided a useful review of the then state-of-the-art in engineering computational methods. The performance of a range of Navier-Stokes solvers was compared with that of the viscous/inviscid coupled methods currently being used by the aerospace industry for design purposes. The results of the Workshop indicated that, indeed, the Navier-Stokes solvers were able to deal in a routine manner, at least qualitatively, with transonic flows involving shock-induced and trailing-edge separations. These are flow regimes in which viscous/inviscid coupled methods such as VGK[2] and GRUMFOIL[3] tend to break down.

The majority of existing transonic flow solvers for the Reynolds-averaged Navier-Stokes equations at present employ the algebraic Baldwin-Lomax[4] turbulence model or the hybrid model due to Johnson and King[5]. Experience indicates that the Baldwin-Lomax model gives reasonable predictions for fully-attached flow situations, but poor results in the presence of shock-induced separation. The Johnson-King model has been devised specifically to deal with shock-separated flows, and the results presented by King[6] and Coakley[7] at the AIAA Workshop show substantial improvements in predictions for the shock wave/boundary layer interaction region. The model does, however, introduce discrepancies in lower surface pressure distributions which are reflected in the resulting lift-drag polars at high-lift conditions. Also, the general applicability of the Johnson-King model to geometries more complex than simple aerofoils or wings is ultimately limited by the thin-shear layer assumption within its formulation and the use of an eddy viscosity to model the Reynolds stresses.

As discussed by Launder[8], eddy-viscosity based turbulence models, including the one- and two-equation models which

solve additional modelled turbulence transport equations, give reasonable results only for flows close to local equilibrium conditions. Also, it is known from experiments that the Reynolds stresses are highly-sensitive to surprisingly small extra rates of strain. This behaviour is not reflected by eddy viscosity models, which are insensitive to the effects of streamline curvature, for example, unless ad-hoc modifications are introduced. For transonic aerofoil flows, the shock wave/boundary layer interaction is generally under-predicted, even when the flow remains fully-attached and, again, this can be attributed to deficiencies in turbulence modelling at the eddy-viscosity level. Experience in the computation of complex *incompressible* flows[8] suggests that turbulence closure at the Reynolds-stress model level, in which the Reynolds stresses themselves are retained within the mean-flow equations, should lead to improved physical modelling of the anisotropic development of the Reynolds stresses through the shock wave/boundary layer interaction region.

The paper begins by presenting the mean-flow equations governing two-dimensional viscous transonic flows. This is followed by a short review of the various turbulence-modelling options available for potential use with flow solvers based on the Reynolds-averaged Navier-Stokes equations. The main features of a recently-developed flow solver employing a one-equation turbulence model are then described. The results of an extensive evaluation of the method are discussed next, covering a wide range of transonic flow conditions for the Boeing BAC I aerofoil, a typical modern supercritical section. These results are used to indicate some of the inherent limitations associated with turbulence modelling at the eddy-viscosity level. The paper closes with some proposals regarding the most profitable near-term way forward to achieving an improved predictive capability for viscous transonic aerofoil flows.

Governing Mean-Flow Equations

It is assumed that the viscous transonic flow development around aerofoil sections is governed by the compressible Reynolds-averaged Navier-Stokes equations, written in terms of mass-weighted average variables. Transonic flows involve regions of supersonic flow, usually terminated by shock waves, embedded within an outer subsonic compressible flow domain. The steady-state Reynolds-averaged Navier-Stokes equations change their mathematical nature, from elliptic to hyperbolic, in crossing from subsonic to supersonic flow regions. The resulting complexity of numerical treatment can be circumvented by considering the unsteady form of the equations, and using a numerical procedure which marches in time to steady-state solutions. Therefore, the governing mean-flow equations are put into the following time-dependent integral form, to facilitate the subsequent development of a suitable numerical solution procedure

$$\frac{\partial}{\partial t}\int_{\Omega} \underline{W}\, d\Omega + \int_{\Omega_s} \underline{H}.\underline{n}\, d\Omega_s = 0 \qquad (1)$$

Ω is the two-dimensional flow domain, Ω_s is the boundary to the domain and $\underline{n}$ is the unit outward normal to this boundary. The contour integration around the boundary Ω_s is taken in the anticlockwise sense. $\underline{W}$ is the vector of conserved mean-flow variables

$$\underline{W} = \begin{bmatrix} \rho \\ \rho U \\ \rho V \\ \rho E \end{bmatrix} \qquad (2)$$

where U and V are the cartesian mean-velocity components, ρ is the density and E is the total energy per unit mass. $\underline{H}$ contains the flux vectors

$$\underline{H} = \underline{F}.\underline{i} + \underline{G}.\underline{j} = (\underline{F}^i + \underline{F}^v).\underline{i} + (\underline{G}^i + \underline{G}^v).\underline{j} \qquad (3)$$

$\underline{i}$ and $\underline{j}$ being unit vectors in the X and Y directions of the cartesian coordinate system. The flux vectors $\underline{F}$ and $\underline{G}$ include both inviscid convective transport and viscous diffusive transport terms. $\underline{F}^i$ and $\underline{G}^i$ are the convective flux vectors

$$\underline{F}^i = \begin{bmatrix} \rho U \\ \rho U^2 + P \\ \rho UV \\ \rho UH \end{bmatrix}, \quad \underline{G}^i = \begin{bmatrix} \rho V \\ \rho UV \\ \rho V^2 + P \\ \rho VH \end{bmatrix} \qquad (4)$$

P is the static pressure and H the total enthalpy per unit mass. $\underline{F}^v$ and $\underline{G}^v$ are the viscous diffusive flux vectors

$$\underline{F}^v = \begin{bmatrix} 0 \\ \sigma_{xx} \\ \sigma_{xy} \\ U\sigma_{xx} + V\sigma_{xy} + q_x \end{bmatrix},$$

$$\underline{G}^v = \begin{bmatrix} 0 \\ \sigma_{xy} \\ \sigma_{yy} \\ U\sigma_{xy} + V\sigma_{yy} + q_y \end{bmatrix} \qquad (5)$$

σ_{xx}, σ_{yy} and σ_{xy} are components of the stress tensor, which contain contributions from the molecular viscosity μ and the Reynolds stresses

$$\sigma_{xx} = -\mu s_{xx} + \overline{\rho u^2}, \quad \sigma_{yy} = -\mu s_{yy} + \overline{\rho v^2},$$
$$\sigma_{xy} = -\mu s_{xy} + \overline{\rho uv} \qquad (6)$$

where the components of the mean-strain tensor are

$$s_{xx} = 2\frac{\partial U}{\partial X} - \frac{2}{3}\left[\frac{\partial U}{\partial X} + \frac{\partial V}{\partial Y}\right],$$

$$s_{yy} = 2\frac{\partial V}{\partial Y} - \frac{2}{3}\left[\frac{\partial U}{\partial X} + \frac{\partial V}{\partial Y}\right],$$

$$s_{zz} = -\frac{2}{3}\left[\frac{\partial U}{\partial X} + \frac{\partial V}{\partial Y}\right], \quad s_{xy} = \left[\frac{\partial U}{\partial Y} + \frac{\partial V}{\partial X}\right] \qquad (7)$$

Similarly, q_x and q_y are components of the heat-flux vector, containing contributions from the molecular viscosity and turbulent heat-flux terms

$$q_x = -\frac{\gamma\mu}{Pr}\frac{\partial T}{\partial X} + \gamma\,\overline{\rho tu}, \quad q_y = -\frac{\gamma\mu}{Pr}\frac{\partial T}{\partial Y} + \gamma\,\overline{\rho tv} \qquad (8)$$

The molecular viscosity μ is evaluated using Sutherland's law, the static temperature T having been obtained previously from the equation of state

$$P = (\gamma - 1)\rho T \qquad (9)$$

Pr and γ in equation (8) are the laminar Prandtl number and ratio of specific heats, and take constant values of 0.72 and 1.4 respectively for air. The surface boundary conditions for equation (1) are the no-slip conditions, together with the assumption of an adiabatic wall

$$U_w = V_w = \left[\frac{\partial T}{\partial y_n}\right]_w = \left[\frac{\partial P}{\partial y_n}\right]_w = 0 \qquad (10)$$

Subscript w denotes conditions at the wall and y_n is the surface normal distance.

The mean-flow equations do not form a closed system, this being due to the time-averaging procedures used in their derivation. The Reynolds stresses in equation (6) and the turbulent heat-flux terms in equation (8) must be modelled in terms of known or knowable quantities before the set of mean-flow equations can be solved. This is known as the turbulence closure problem, and it is the role of the turbulence model to provide the necessary closure.

Turbulence Modelling

The range of turbulence-modelling options that are currently available for use with the compressible Reynolds-averaged Navier-Stokes equations are discussed briefly in this section. Attention is restricted to models that can be readily incorporated into numerical methods for use in a practical engineering environment. It should be noted that, to date, not all of these turbulence model variants have been applied to transonic external aerodynamic flows.

Differential Stress Model

As indicated above, the role of the turbulence model is to supply the local values of the various Reynolds stresses throughout the flow domain, in order to close the set of mean-flow equations. The exact Navier-Stokes equations governing the instantaneous flow development can be manipulated to produce a set of exact transport equations for the Reynolds stresses. These equations can be written in the following symbolic form

$$\frac{\partial \overline{\rho u_i u_j}}{\partial t} + C_{ij} - D_{ij} = P_{ij} + \Phi_{ij} - \epsilon_{ij} \qquad (11)$$

A similar set of equations can be derived governing the transport of the turbulent heat fluxes in equation (8). The physical processes represented by the various terms in equation (11) are (reading from left to right): time rate of change of the Reynolds stresses; convective transport; diffusive transport; production; stress re-distribution; viscous dissipation (destruction). Turbulence closure at the Differential Stress Model level involves solution of modelled forms of the Reynolds stress transport equations in conjunction with the mean-flow equations. Modelling of equation (11) is required because the terms D_{ij}, Φ_{ij} and ϵ_{ij} contain additional unknown quantities. However, C_{ij} and P_{ij}, the convective transport and production terms, can be handled *exactly* without any modelling assumptions. This is the most significant advantage of the Differential Stress Model approach to turbulence closure compared to the simpler eddy-viscosity based models discussed below. Use of equation (11) leads to a subtle interaction between the various components of the Reynolds stress tensor and the mean flowfield, resulting in a strong sensitivity to small extra rates of strain, such as those due to streamline curvature.

The use of equation (11) as the basis of a turbulence model requires the solution of a further modelled transport equation, for a local turbulent length scale or time scale. Therefore, a total of five turbulence transport equations and four mean-flow equations need to be solved, even if the mean flowfield is two-dimensional. Most practical applications of equation (11), mainly to complex *incompressible* internal flows, have been based on the modelling proposals of Launder et al[9]. Recent developments in turbulence modelling at this level are discussed by Launder[8], and a comprehensive review of modelling proposals for the important near-wall region is given by So et al[10].

Eddy Viscosity Models

It is obviously computationally expensive to solve a total of nine mean-flow and turbulence transport equations when the mean flow itself is two-dimensional in nature. A range of more simple turbulence models can be devised by invoking the Boussinesq approximation, which models the Reynolds stresses by analogy with the laminar viscous stress terms in equation (6). Thus, the Reynolds stresses appearing in the mean-flow equations are replaced by the following relations, involving a single *scalar* turbulent (or eddy) viscosity coefficient μ_t

$$\overline{\rho u^2} = -\mu_t s_{xx} + \frac{2}{3}\rho k, \quad \overline{\rho v^2} = -\mu_t s_{yy} + \frac{2}{3}\rho k,$$

$$\overline{\rho w^2} = -\mu_t s_{zz} + \frac{2}{3}\rho k, \quad \overline{\rho uv} = -\mu_t s_{xy} \qquad (12)$$

where k is the turbulent kinetic energy, defined as one-half the sum of the three Reynolds normal stresses

$$\rho k = \frac{1}{2}(\overline{\rho u^2} + \overline{\rho v^2} + \overline{\rho w^2}) \qquad (13)$$

Similarly, the turbulent heat-flux terms in equation (8) are modelled using the turbulent viscosity coefficient, by introduction of a turbulent Prandtl number Pr_t

$$\overline{\rho tu} = -\frac{\mu_t}{Pr_t}\frac{\partial T}{\partial X}, \quad \overline{\rho tv} = -\frac{\mu_t}{Pr_t}\frac{\partial T}{\partial Y} \qquad (14)$$

The turbulence closure problem now reduces to that of specifying local values of a single variable, μ_t, instead of the four Reynolds stresses. This decrease in turbulence model complexity is gained at the expense of the explicit modelling of the physical processes involved in the transport of the Reynolds stresses. Since μ_t is a scalar quantity, much of the vector behaviour of the Reynolds stresses is lost by introduction of the Boussinesq approximation.

On dimensional grounds, the turbulent viscosity coefficient can be expressed in terms of local velocity and length scales, and it is generally assumed that single scales are sufficient to characterise the turbulent flowfield

$$\mu_t = \rho V_\mu L_\mu \qquad (15)$$

Turbulence models of algebraic, one-equation or two-equation type can be devised, depending on the way in which V_μ and L_μ are to be obtained. For one- and two-equation models, it is usual to define the local turbulent velocity scale using the turbulent kinetic energy k, another scalar quantity

$$V_\mu = k^{1/2} \qquad (16)$$

An exact transport equation for k can be derived by summation of the three Reynolds normal stress transport equations, and written in symbolic form as

$$\frac{\partial \rho k}{\partial t} + C_k - D_k = P_k + \Phi_k - \rho\epsilon \qquad (17)$$

The various symbols in equation (17) represent similar physical processes to those described above for equation (11), the individual Reynolds stress transport equations. However, unlike P_{ij} in equation (11), the production term P_k can no longer be treated in an exact manner since it involves the Reynolds stresses, which have now been modelled using the turbulent viscosity coefficient.

The length scale L_μ in the turbulent viscosity relation, equation (15) must now be determined. One option is to model ϵ, the dissipation rate of k in equation (17), by defining a dissipation length scale L_ϵ

$$L_\epsilon = k^{3/2} / \epsilon \qquad (18)$$

L_μ can be taken equal to L_ϵ over most of the flowfield, apart from in the molecular viscosity dominated region immediately adjacent to solid walls. A one-equation turbulence model is obtained, solving a modelled transport equation for k, if the length scales L_μ and L_ϵ are specified in algebraic form. This approach may lead to specification problems for flows more complex than simple thin-shear layers. The alternative is to solve a further equation for a second turbulence quantity which can be related to a length scale. The popular two-equation k-ϵ model of Launder and

Spalding[11] employs a modelled transport equation for ϵ, the dissipation rate of k, with the required length scale being obtained using equation (18). There are numerous variants of two-equation turbulence models, and these are reviewed by Patel et al[12] and Speziale et al[13]. These differ mainly in the way that the near-wall region is treated.

Algebraic Stress Model

Most of the physical modelling benefits of the Differential Stress Model can be incorporated into a one- or two-equation model framework if the time rate of change and transport terms in the Reynolds stress equations are approximated by the equivalent terms in the turbulent kinetic energy transport equation, as follows

$$\frac{\partial \overline{\rho u_i u_j}}{\partial t} + C_{ij} - D_{ij} = \frac{\overline{\rho u_i u_j}}{\rho k}\left[\frac{\partial \rho k}{\partial t} + C_k - D_k\right] \qquad (19)$$

Combining this approximation with equations (11) and (17), in suitably modelled forms, leads to a set of *algebraic* relations for the Reynolds stresses

$$\overline{\rho u_i u_j} = \rho k\,(P_{ij} + \Phi_{ij} - \epsilon_{ij})/(P_k + \Phi_k - \rho\epsilon) \qquad (20)$$

The Boussinesq assumption of a turbulent viscosity coefficient can now be dropped and the Reynolds stresses re-introduced explicitly into the mean-flow equations. The term Algebraic Stress Model is somewhat misleading in this context since *differential* transport equations for k and ϵ (or k alone for a one-equation formulation) need to be solved in conjunction with the above algebraic Reynolds stress relations.

Algebraic and Hybrid Models

An algebraic turbulence model is obtained if the velocity and length scales V_μ and L_μ in the turbulent viscosity relation, equation (15), are specified in terms of mean-flow quantities only. The most popular of such models is that due to Baldwin and Lomax[4], which is essentially a mixing length model modified to be compatible with Navier-Stokes solvers. It can be shown that such a mixing length formulation is equivalent to neglecting all terms, apart from the production and dissipation terms, in the transport equation for the turbulent kinetic energy, equation (17). Thus, no account is taken of convective or diffusive transport processes within the model. Physically, this amounts to an assumption of local turbulence equilibrium, with turbulence energy being created and destroyed at the same position in the flowfield.

It is highly-improbable that the turbulence remains in local equilibrium through shock wave/boundary layer interactions, and upstream turbulence history effects are likely to have a significant influence on the subsequent flow development, particularly if shock-induced separation occurs. Johnson and King[5] re-introduce such an upstream influence by solving an *ordinary* differential equation for the maximum shear stress across the viscous layer, using this to define the velocity scale in the turbulent viscosity relation, equation (15). For this reason, the Johnson-King model is perhaps better termed a hybrid model, to distinguish it from the pure algebraic models such as that of Baldwin and Lomax. King[6] and Coakley[7] demonstrate significantly-improved predictions of shock wave strength and position for transonic aerofoil flows involving shock-induced separation. However, there are discrepancies in lower surface pressure distributions, the cause of which is unclear at present. The Johnson-King model also retains many of the physical modelling limitations associated with the use of a scalar turbulent viscosity coefficient and a thin-shear layer formulation. Whilst being well-suited for use in predicting transonic aerofoil and wing flows, it is unlikely that the model can be adapted for application to more complex interacting flow situations.

Computational Method

The computational method used for the present study has been developed specifically to investigate issues associated with turbulence model implementation and evaluation for viscous transonic flows. A detailed description of the method, together with an initial evaluation for a number of transonic aerofoil sections, is given by Johnston[14]. The capability to deal with more complex geometries, such as multi-element high-lift aerofoils, is incorporated within the method by adopting a block-structured computational grid formulation. This two-dimensional method is also being used as a 'pathfinder' for a three-dimensional method which is currently under active development.

The two-dimensional compressible Reynolds-averaged Navier-Stokes equations are solved in time-dependent integral form, see equation (1). A simple, but relatively efficient, numerical scheme is adopted for the mean-flow equations, so that effort can be concentrated on the turbulence modelling aspects. Thus, a cell-centred, finite-volume spatial discretisation of the flow equations is employed, with steady-state solutions being obtained by marching in time using an explicit multi-stage scheme. The main features of the present numerical method are summarized in this section, which also includes discussion of the progress made in the implementation of a range of turbulence modelling options. The results presented in the subsequent section are used to illustrate the quality of predictions that can be obtained when using a turbulent viscosity coefficient to model the Reynolds stresses.

Spatial Discretisation

The computational domain Ω is divided into a finite number of non-overlapping quadrilateral cells. Fig 1 shows a typical cell, which has four edges (1,2,3,4) and four vertices (a,b,c,d). The conserved variables, equation (2), within a cell are represented by their average cell-centre values, such quantities being denoted by suffices (i,j) in the local curvilinear coordinate directions (ξ,η). The governing mean-flow equations are applied to each computational cell in turn, and equation (1) becomes

$$\frac{\partial \underline{W}_{i,j}}{\partial t} = -\frac{1}{h_{i,j}} \int_{\Omega_c} (\underline{F}\, dY - \underline{G}\, dX) \qquad (21)$$

where Ω_c refers to a contour integration around the boundary of the cell, which has an area of $h_{i,j}$. Performing the finite-volume spatial discretisation of equation (21) before the time discretisation leads to a large set of ordinary differential equations with respect to time

$$\frac{d\underline{W}_{i,j}}{dt} = -\frac{1}{h_{i,j}} \sum_{k=1}^{4} (\underline{F}_k\, \Delta Y_k - \underline{G}_k\, \Delta X_k) \qquad (22)$$

The summation (k) is over the four edges of the cell, Fig 1, where

$$\Delta X_1 = X_a - X_d\,, \quad \Delta X_2 = X_b - X_a\,,$$

$$\Delta X_3 = X_c - X_b\,, \quad \Delta X_4 = X_d - X_c \quad \text{etc} \qquad (23)$$

Cell-edge values of the flux terms $\underline{F}$ and $\underline{G}$ in equation (3) are approximated by averaging the two adjacent cell-centre values

$$\underline{F}_1 = (\underline{F}_{i,j} + \underline{F}_{i,j-1}) / 2 \quad \text{etc} \qquad (24)$$

The viscous flux terms in equation (5) require cell-edge values of first derivatives of U, V and T with respect to X and Y. Derivatives at the cell vertices (a,b,c,d) are calculated using auxiliary cells surrounding each vertex, Fig 2. For example, a discrete application of the divergence theorem to

the auxiliary cell surrounding vertex b results in

$$\left[\frac{\partial U}{\partial X}\right]_b = \frac{1}{h_b}\sum_{k=5}^{8} U_k\,\Delta Y_k\ ,$$

$$\left[\frac{\partial U}{\partial Y}\right]_b = -\frac{1}{h_b}\sum_{k=5}^{8} U_k\,\Delta X_k \qquad (25)$$

where h_b is the area of the auxiliary cell. Cell-edge mean velocities can be approximated by the relevant cell-centre values

$$U_5 = U_{i+1,j}\ ,\ U_6 = U_{i+1,j+1} \quad \text{etc} \qquad (26)$$

The cell-edge values of the derivatives are then approximated by

$$\left[\frac{\partial U}{\partial X}\right]_1 = \frac{1}{2}\left[\left[\frac{\partial U}{\partial X}\right]_a + \left[\frac{\partial U}{\partial X}\right]_d\right] \quad \text{etc} \qquad (27)$$

Non-reflecting farfield boundary conditions are applied at the outer boundary to the computational domain. These are constructed using the Riemann invariants for a one-dimensional flow normal to the outer boundary.

Solution Procedure

Additional numerical dissipative terms must be added to the discretised mean-flow equations, in order to suppress the odd-even point de-coupling behaviour associated with the centred treatment of convection terms, and to ensure clean capture of shock waves. These terms are formulated in an identical way to that described by Jameson et al[15] for the Euler equations. However, particular attention must be paid to controlling the magnitude of the numerical dissipation within boundary layer and wake regions, so that the physical (molecular and turbulent) viscosity is not swamped by the numerics; see Johnston[14] for the approach adopted in the present numerical method. Finally, the resulting semi-discrete mean-flow equations are marched in time to a steady-state solution using an explicit multi-stage scheme[15].

Turbulence Modelling

Turbulent-viscosity based models are being used for the initial validation and evaluation of the present numerical method, and three levels of turbulence modelling have been implemented to date: the algebraic Baldwin-Lomax model; a one-equation model; a two-equation high-Reynolds number k-ϵ model with a one-equation near-wall formulation. The Baldwin-Lomax model was used only during the early stages of validation[14,16]. Subsequent work has concentrated on a detailed evaluation of the one-equation turbulence model[17,18] and the present paper is a continuation of this evaluation process. As explained above, a one-equation model involves solution of a modelled transport equation for the turbulent kinetic energy k, equation (17), together with algebraic specifications for the two turbulent length scales L_μ and L_ϵ, equations (15) and (18). The turbulent kinetic energy transport equation can be written in a time-dependent integral form, similar to equation (1) for the mean-flow equations, as follows

$$\frac{\partial}{\partial t}\int_{\Omega} \underline{W}\ d\Omega + \int_{\Omega_S} \underline{H}.\underline{n}\ d\Omega_S + \int_{\Omega} \underline{S}^V\ d\Omega = 0 \qquad (28)$$

The principal difference is the inclusion of a source term $\underline{S}^V$, which represents all the terms in equation (17) not involving convective and diffusive transport. Full details of the formulation and implementation of the one-equation turbulence model used in the present numerical method are given by Johnston[14].

The use of a transport equation for the turbulent kinetic energy leads to an upstream influence of the turbulence on the mean-flow development via the turbulent viscosity coefficient μ_t. Predictions comparable with the Johnson-King model might therefore be expected. In fact, as will be seen below, experience to date indicates that this does not appear to be the case. This is perhaps an unexpected result, since the ordinary differential equation for the maximum shear stress, used by the Johnson-King model to prescribe the turbulent velocity scale, is obtained by modelling of the turbulent kinetic energy transport equation. Further investigation of these discrepancies in performance between the two turbulence models is required.

Results

The results presented in this section were obtained by using the present numerical method in a 'production' mode, with a fixed set of flow algorithm parameters and the one-equation turbulence model. The computational grid, of C-type topology, was generated using algebraic procedures and is of multi-block form. Fig 3 shows the block structure of the grid, together with the number of computational cells in the two curvilinear directions ξ and η; see Fig 1. Thus, there are 224 cells wrapped around the aerofoil surface, 64 cells in the near surface-normal and cross-wake directions, and 24 cells from the trailing edge to the downstream boundary. The initial near-wall cell spacings are 0.002 and 0.00005 chords respectively in the two curvilinear directions, the latter being sufficiently close to the surface to enable an accurate evaluation of the skin friction. The outer boundary to the computational domain is 15 chords away from the aerofoil surface and 10 chords downstream of the trailing edge.

RAE 2822 Aerofoil

The RAE 2822 aerofoil section has a maximum thickness of 12.1% and a sharp trailing edge. Cook et al[19] present detailed experimental data for this aerofoil for a range of transonic flow conditions, taken from tests in the 8ft x 6ft transonic wind tunnel at RAE Farnborough. The data includes surface pressure distributions, mean-velocity profiles, integral thicknesses and skin friction measurements, making this one of the most complete data-sets available for validation of numerical methods. The aerofoil geometry and the inner region of the computational grid used for the present study are shown in Fig 4. The manufactured geometry of the aerofoil model is used for the computations and transition is fixed at 3% chord on the upper and lower surfaces, in accordance with experiment. Results are presented for one flow condition only, Case 9, to illustrate the level of agreement with experiment typically achieved for cases involving fully-attached flow conditions. The freestream Mach number M, Reynolds number R and corrected incidence angle α are 0.73, 6.5×10^6 and 2.79° respectively; see Cook et al[19] for the correction applied to α for tunnel wall interference effects.

The predicted distributions of surface pressure coefficient, upper surface skin friction coefficient and upper surface integral thicknesses (δ^* and θ being the displacement and momentum thicknesses respectively) are compared with experiment in Fig 5. An overall satisfactory level of agreement with experiment is achieved, the main differences appearing in the recovery region downstream of the shock wave. In particular, Fig 5(a) indicates that the predicted shock wave is 'too inviscid' and there are also detailed discrepancies in the shape of the mean-velocity profiles (not shown here) in this downstream region. The predicted lift, drag and pitching moment coefficients of 0.830, 0.0180 and -0.0945 compare reasonably-well with the experimental values of 0.803, 0.0168 and -0.099. The over-prediction of the total

drag coefficient by 12 drag counts can be attributed to an over-prediction of the wave drag contribution, due to the stronger shock wave present in the computations.

Boeing BAC I Aerofoil

Johnson and Hill[20] present surface pressure distributions and integrated loads for the Boeing BAC I aerofoil section, covering an extended range of transonic flow conditions. The aerofoil was tested in the NASA Langley 0.3-Meter Transonic Cryogenic Tunnel, as part of the NASA/US industry Advanced Technology Airfoil Tests (ATAT) programme; see Ladson and Ray[21] for further details of this programme. The Boeing BAC I aerofoil has a maximum thickness of 10% chord and a trailing-edge base thickness of 0.202% chord. This blunt base has been closed down to a sharp trailing edge for the computations, by small modifications to the design geometry of the upper and lower surfaces. Since the base thickness is small, these slight changes in geometry are expected to have little effect on the predictions. Fig 6 shows the Boeing BAC I aerofoil section and the inner region of the computational grid.

Results are presented in this section for three nominal freestream Mach numbers at a Reynolds number R of 7.7 x 10^6, with transition fixed at 10% chord on the upper and lower surfaces as in the experiment. The incidence angles α in the original data report of Johnson and Hill[20] have been corrected for lift-induced interference effects using the following relation

$$\Delta\alpha = -1.721\ C_L \qquad (29)$$

quoted by Jenkins[22], where C_L is the lift coefficient and α is in degrees.

Incidence sweep at M = 0.70

Fig 7 shows selected surface pressure distributions for Langley run 9, at a nominal freestream Mach number M of 0.70. The predictions are in reasonably-good agreement with experiment for the first four data points, the computations indicating fully-attached flow for these cases. The upper surface suction levels are under-predicted over the front part of the aerofoil. This may be associated with equation (29) slightly over-correcting the incidence angle, although the rest of the pressure distribution agrees well with experiment. Another possibility is the influence of the boundary layers growing on the sidewalls of the wind tunnel. Jenkins[22] discusses the need for a decrease in the nominal freestream Mach number to take such an effect into account, but this would also lead to a significant upstream movement of the shock wave position. The use of a sidewall correction to the Boeing BAC I aerofoil data-set is currently under discussion with the data originators, and further investigation is required.

Shock-induced separation is predicted for data points 15 and 16, covering a chordwise extent of $0.45 < X/c < 0.51$ and $0.45 < X/c < 0.56$ respectively, with trailing-edge separation also predicted for data point 16 beyond X/c = 0.98. Note the large upstream movement and weakening of the shock wave between data points 15 and 16 in the experiment, indicating the presence of significant shock-induced separation. This behaviour is not reflected in the computations, which predict a much stronger shock wave further downstream for data point 16. The reluctance of the computed shock wave to move upstream and weaken appears to be a characteristic of computations using turbulence models based on a turbulent viscosity coefficient, and Johnston[14] shows similar results for other aerofoil sections.

Incidence sweep at M = 0.76

Fig 8(a) shows that the slight under-prediction of upper surface suction levels also occurs at the higher freestream Mach number of 0.76, for Langley run 8. Further, there is now a significant discrepancy between the computed and experimental shock wave position for data point 8, which is a fully-attached flow condition. Shock-induced separation is predicted between $0.645 < X/c < 0.67$ for data point 10, and from X/c = 0.645 to the trailing edge for data point 12. Again, the computations do not reflect the upstream movement and weakening of the shock wave between these two data points.

The predicted variations of integrated loads for the incidence angle sweep are compared with experiment in Fig 8(b) to (d), these plots also including repeat measurements from Langley run 10. The lift-curve slope appears to be slightly over-predicted, with the greatest discrepancies at the negative incidence angles. This may indicate an over-prediction by equation (29) of the lift-interference correction at lower lift levels. The computed lift coefficient does not reach a maximum at high incidence, as in the experiment, presumably due to the incorrect predicted behaviour of the shock wave/boundary layer interaction in the presence of shock-induced separation. Fig 8(c) shows that the lift-drag polar is very well-predicted, despite the detailed differences between computed and measured surface pressure distributions for the individual data points. There is less satisfactory agreement for the lift-pitching moment polar, Fig 8(d), which is much more sensitive to the discrepancies in the computed shock wave position.

Incidence sweep at M = 0.80

The final set of comparisons presented are for Langley run 7 at a nominal freestream Mach number of 0.80, Fig 9. The shock wave is predicted consistently downstream of experiment for all of the data points shown, resulting in an over-prediction of shock wave strength due to the higher suction levels achieved in the computations. Note also, that the agreement with experiment for the lower surface pressure distributions is less satisfactory than for the two lower Mach number incidence angle sweeps. The computations indicate fully-attached flow for the first three data points, but shock-induced separation with no re-attachment for data points 6 to 8. Predicted integrated loads are compared with experiment in Fig 9(b) to (d). The lift coefficient variation with incidence angle is very well-predicted, apart from at the lower lift levels associated with negative incidence angles. Fig 9(c) indicates that premature drag rise is predicted at lower lift levels where the flow is still fully-attached. This is presumably due to an under-prediction of the shock wave/boundary layer interaction at this higher freestream Mach number. The discrepancies between computed and experimental shock wave position lead to the prediction of a much steeper negative slope to the lift-pitching moment polar, Fig 9(d).

Discussion of Results

Consideration of the results for the Boeing BAC I aerofoil section suggests that the simple correction to incidence angle implied by equation (29) is not sufficient to account for all the tunnel wall interference effects in the experiment. The consistent under-prediction of upper surface suction levels indicates that a negative increment to the nominal freestream Mach number for blockage effects may be required. Whether or not this is due to the influence of the tunnel sidewall boundary layers, as discussed by Jenkins[22] for other aerofoil tests in the same facility, is a matter for further investigation. Despite this uncertainty in the nominal freestream conditions of the experiment, there are larger discrepancies between computations and experiment which must be due to other causes. The general over-prediction of shock wave strength, even at fully-attached flow conditions, indicates that the physical modelling of the shock wave/boundary layer interaction may be deficient. This can

probably be attributed to limitations associated with the use of a scalar turbulent viscosity coefficient to model the Reynolds stresses. Such an approach will not allow the severe streamwise adverse pressure gradient, resulting from the shock wave, to give a sufficiently strong directional bias to the magnitudes of the various Reynolds stress components. In this respect, turbulence closure at the Reynolds stress model level will almost certainly lead to improved predictions.

Conclusions

The main features of a recently-developed numerical method to predict viscous transonic aerofoil flows have been presented. Turbulence modelling is currently at the turbulent viscosity level, and a one-equation model gives results representative of this class of turbulence model. An extensive evaluation of the predictive capability of the method has been carried out using an experimental data-set for the Boeing BAC I aerofoil section. It is concluded that there is a general under-prediction of the shock wave/boundary layer interaction when using a turbulent viscosity coefficient to model the Reynolds stresses in the mean-flow equations. This results in an over-prediction of shock wave strength for freestream Mach numbers beyond 0.76, with a consequent over-prediction of wave drag. The numerical method in its present form is unable to predict the upstream movement and weakening of shock waves when severe shock-induced separation occurs. Nevertheless, some of the quantitative aerodynamic trends for integrated lift, drag and pitching moment coefficients are well-predicted, even with the current formulation of the one-equation turbulence model. Significant improvements in the quantitative predictive capability of the numerical method are anticipated once a Reynolds-stress turbulence closure (either algebraic or differential) is incorporated.

References

1. Holst, T.L., 'Viscous Transonic Airfoil Workshop. Compendium of results', AIAA Paper 87-1460, 1987
2. Collyer, M.R. and Lock, R.C., 'Prediction of viscous effects on steady transonic flow past an aerofoil', Aero Quarterly, Vol 30, August 1979, pp 485/505
3. Melnik, R., Brook, J. and Mead, H., 'GRUMFOIL. A computer code for the computation of viscous transonic flow over airfoils', AIAA Paper 87-0414, 1987
4. Baldwin, B.S. and Lomax, H., 'Thin-layer approximation and algebraic model for separated turbulent flows', AIAA Paper 78-257, 1978
5. Johnson, D.A. and King, L.S., 'A mathematically simple turbulence closure model for attached and separated turbulent boundary layers', AIAA J., Vol. 23, No. 11, November 1985, pp. 1684/1692
6. King, L.S., 'A comparison of turbulence closure models for transonic flows about airfoils', AIAA Paper 87-0418, 1987
7. Coakley, T.J., 'Numerical simulation of viscous transonic airfoil flows', AIAA Paper 87-0416, 1987
8. Launder, B.E., 'Turbulence modelling for the nineties: second moment closure... and beyond?', Lecture Notes in Physics, Vol. 371, 1990, Springer-Verlag, pp. 1/18
9. Launder, B.E., Reece, G.J. and Rodi, W., 'Progress in the development of a Reynolds-stress turbulence closure', J. Fluid Mech., Vol. 68, 1975, pp. 537/566
10. So, R.M.C., Lai, Y.G., Zhang, H.S. and Hwang, B.C., 'Second-order near-wall turbulence closures: a review', AIAA J., Vol. 29, No. 11, November 1991, pp. 1819/1835
11. Launder, B.E. and Spalding, D.B., 'The numerical computation of turbulent flows', Computer Methods in Applied Mechanics and Engineering, Vol. 3, No. 2, 1974, pp. 269/289
12. Patel, V.C., Rodi, W. and Scheuerer, G., 'Turbulence models for near-wall and low Reynolds number flows: a review', AIAA J., Vol. 23, No. 9, September 1985, pp. 1308/1319
13. Speziale, C.G., Abid, R. and Anderson, E.C., 'Critical evaluation of two-equation models for near-wall turbulence', AIAA J., Vol. 30, No. 2, February 1992, pp. 324/331
14. Johnston, L.J., 'Solution of the Reynolds-averaged Navier-Stokes equations for transonic aerofoil flows', Aeronautical Journal, Vol. 95, No. 948, October 1991, pp. 253/273
15. Jameson, A., Schmidt, W. and Turkel, E., 'Numerical solutions of the Euler equations by finite volume methods using Runge-Kutta time-stepping schemes', AIAA Paper 81-1259, 1981
16. Johnston, L.J., 'Computation of viscous transonic aerofoil flows using eddy-viscosity based turbulence models', 7th International Conference on Numerical Methods in Laminar and Turbulent Flow, Stanford, California, USA, 15-19 July 1991
17. Johnston, L.J., 'Transonic aerofoil performance by solution of the Reynolds-averaged Navier-Stokes equations with a one-equation turbulence model', 9th GAMM Conference on Numerical Methods in Fluid Mechanics, September 25-27, 1991, EPFL, Lausanne, Switzerland
18. Johnston, L.J., 'Prediction of the viscous transonic aerodynamic performance of supercritical aerofoil sections', AIAA Paper 92-2653, 10th AIAA Applied Aerodynamics Conference, Palo Alto, California, USA, June 22-24, 1992
19. Cook, P.H., McDonald, M.A. and Firmin, M.C.P., 'Aerofoil RAE 2822 - pressure distributions and boundary layer and wake measurements', AGARD AR 138, May 1979, A6-1 to A6-77
20. Johnson Jr., W.G. and Hill, A.S., 'Pressure distributions from high Reynolds number tests of a Boeing BAC I airfoil in the Langley 0.3-Meter Transonic Cryogenic Tunnel', NASA TM 87600, December 1985
21. Ladson, C.L. and Ray, E.J., 'Status of advanced airfoil tests in the Langley 0.3-Meter Transonic Cryogenic Tunnel', NASA CP 2208, 1981, pp. 37/53
22. Jenkins, R.V., 'Some experience with Barnwell-Sewall type correction to two-dimensional airfoil data', NASA CP 2319, 1984, pp. 375/392

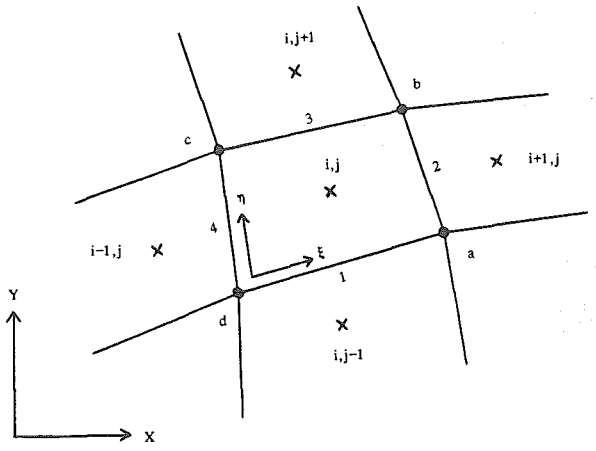

Fig. 1 Notation for main computational cell
x = cell centres; ● = cell vertices

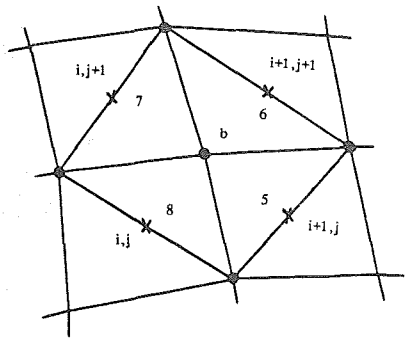

Fig. 2 Auxiliary cell for computation of viscous flux terms

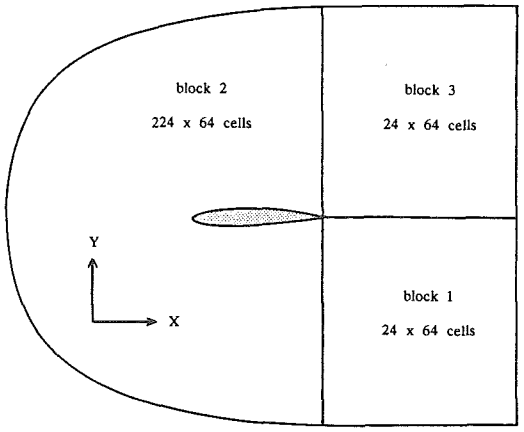

Fig. 3 3-block C-grid structure of computational grid

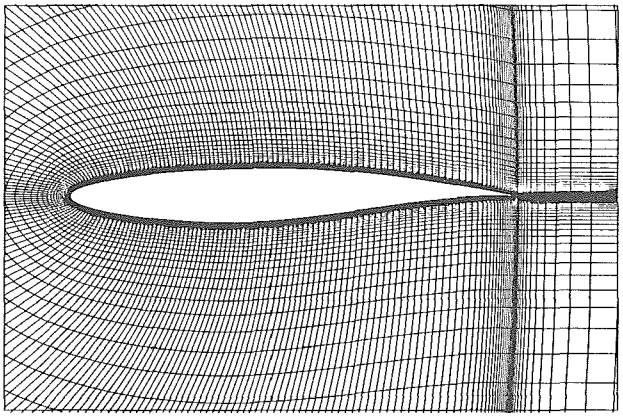

Fig. 4 RAE 2822 aerofoil section and inner region of grid

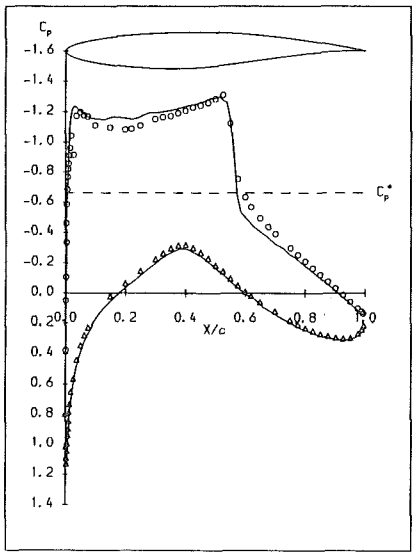

(a) surface pressure distribution

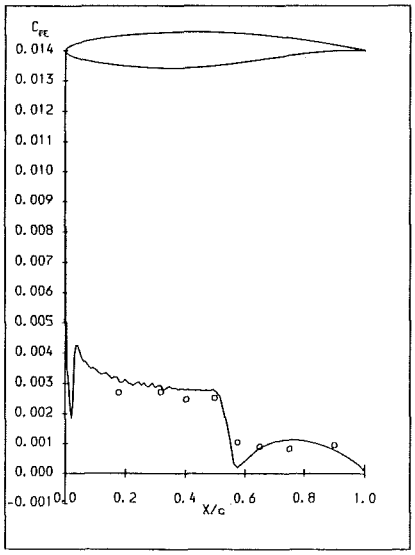

(b) upper surface skin friction

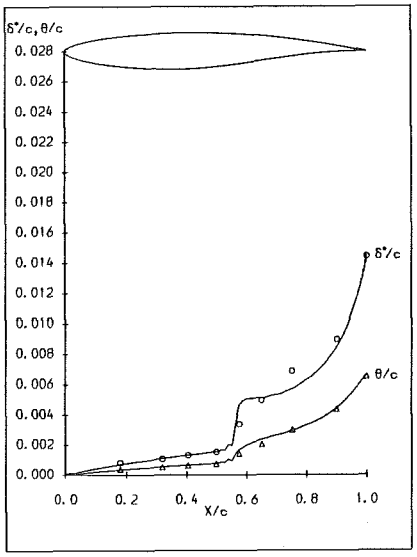

(c) upper surface integral thicknesses

Fig. 5 RAE 2822 - case 9 - M = 0.73 , $\alpha = 2.79^{\circ}$
o,△ experiment; ——— computation

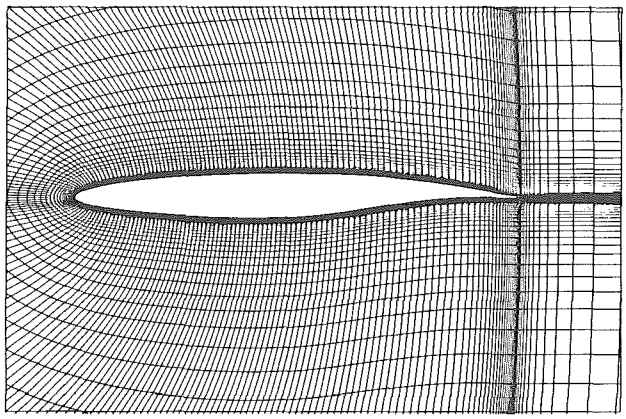

Fig. 6 Boeing BAC I aerofoil section and inner region of grid

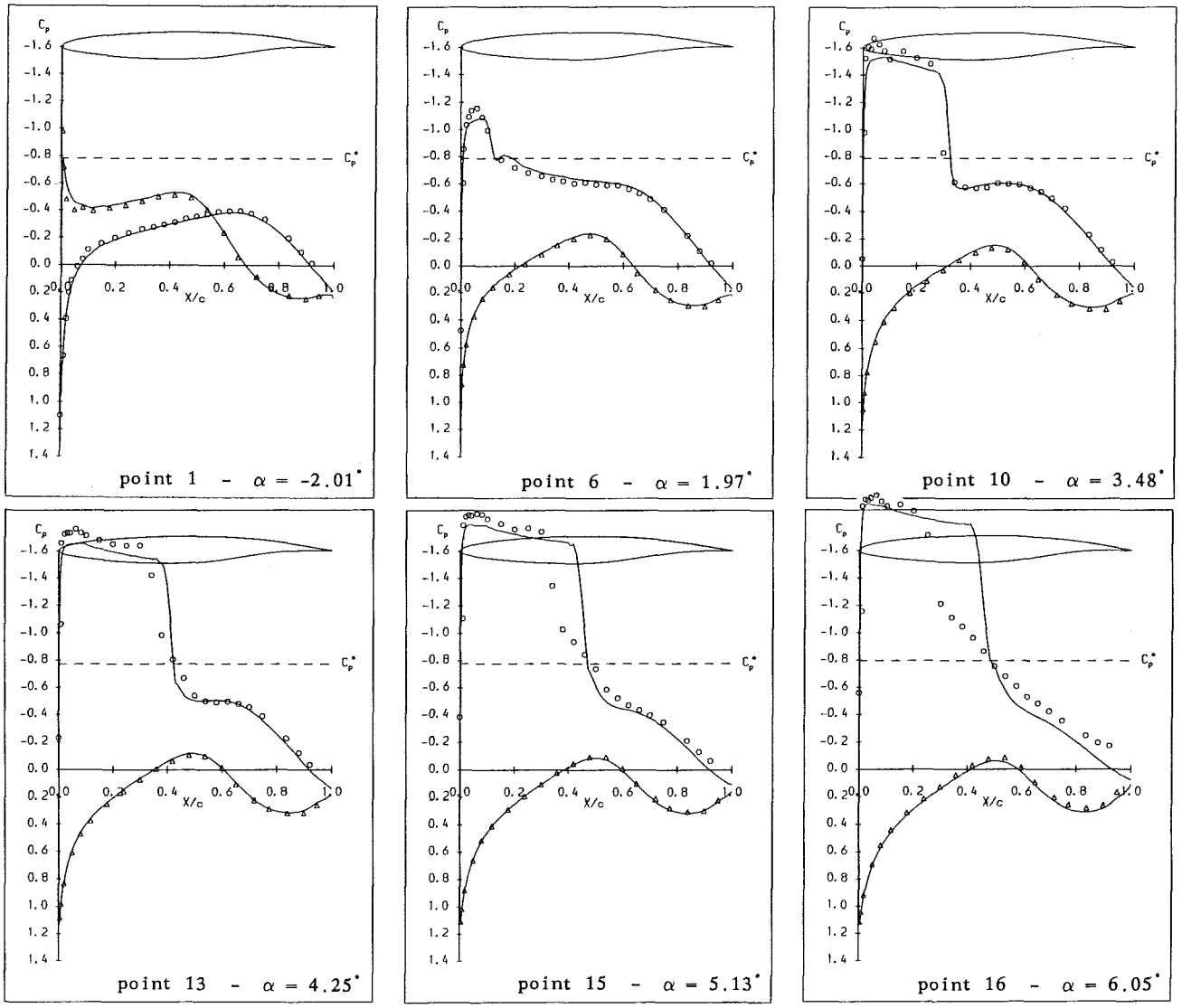

Fig. 7 Boeing BAC I - M = 0.70 , R = 7.7 x 10^6
o,△ experiment; ——— computation

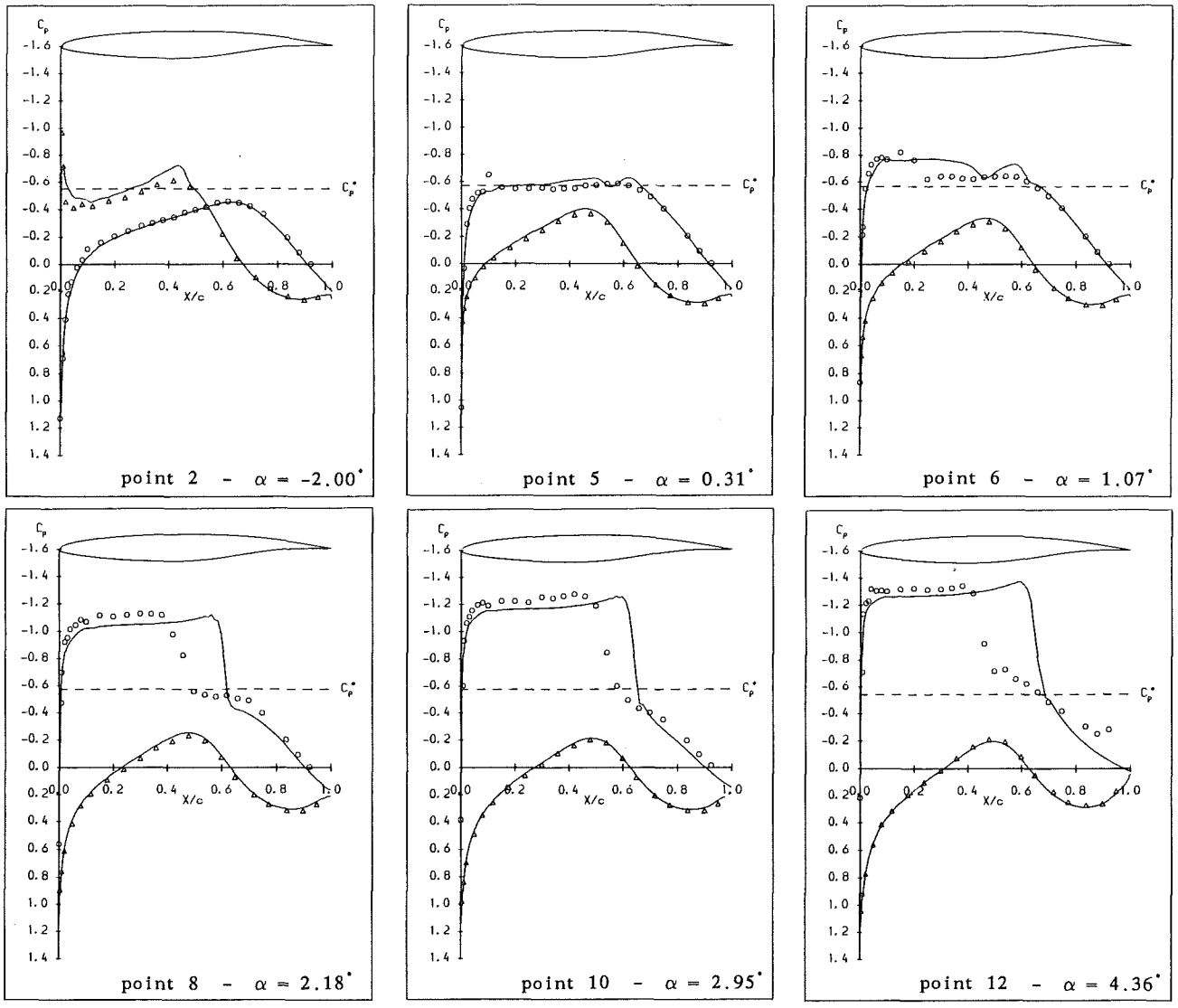

(a) surface pressure distributions

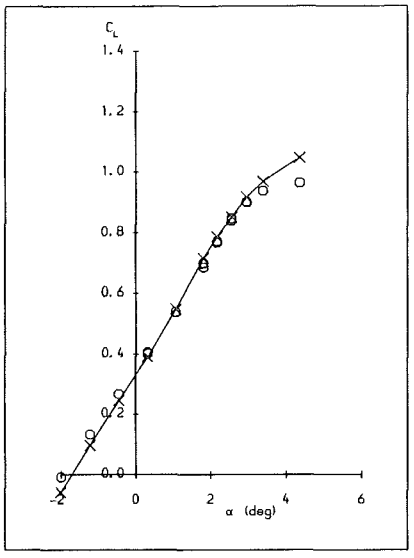

(b) lift vs incidence

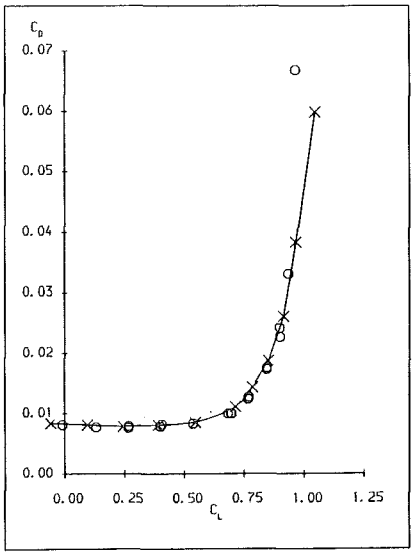

(c) drag vs lift

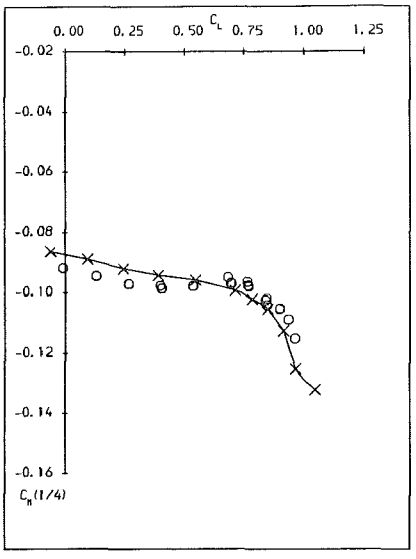

(d) pitching moment vs lift

Fig. 8 Boeing BAC I - M = 0.76 , R = 7.7 x 10^6
o,△ experiment; ——, —×— computation

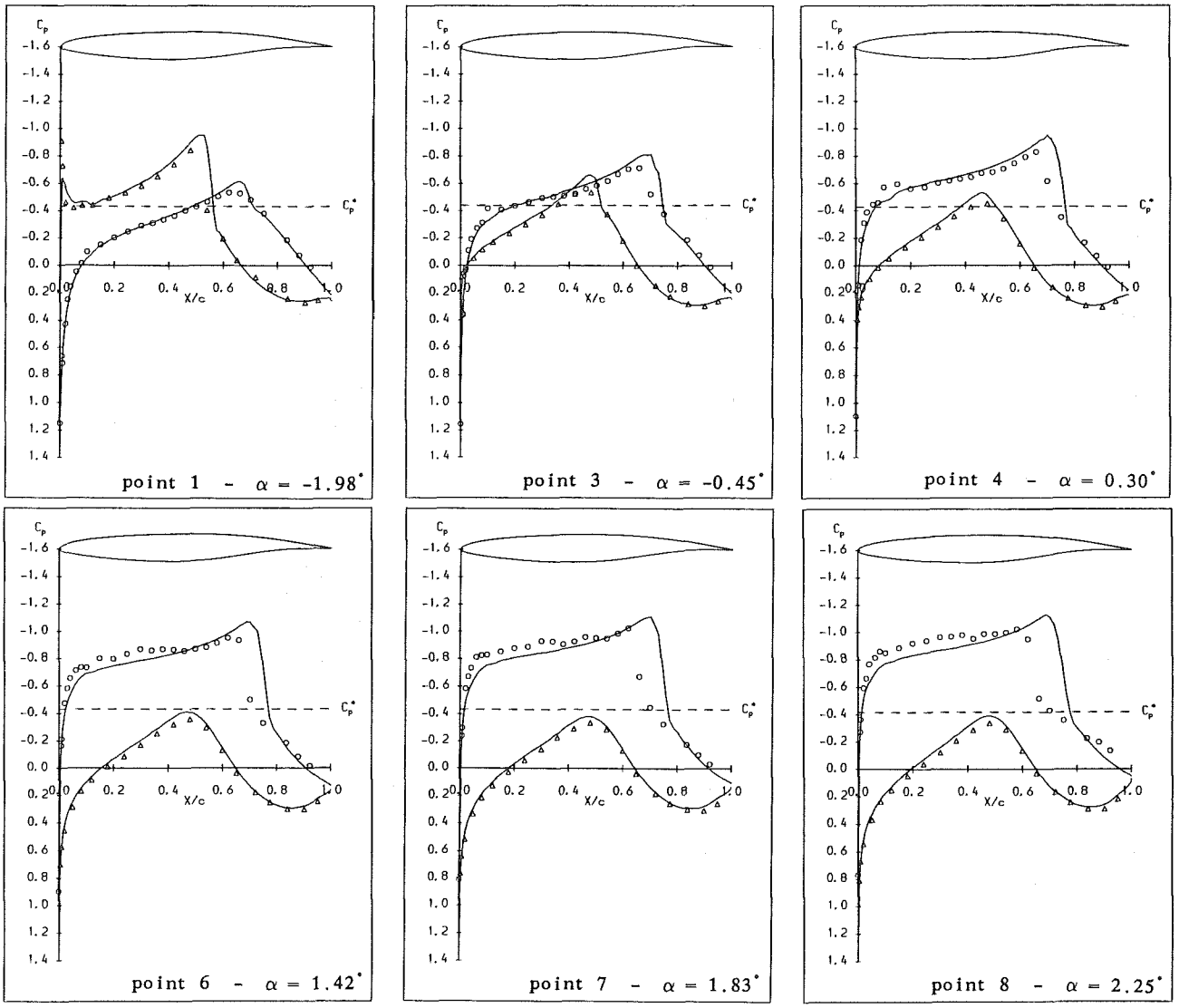

(a) surface pressure distributions

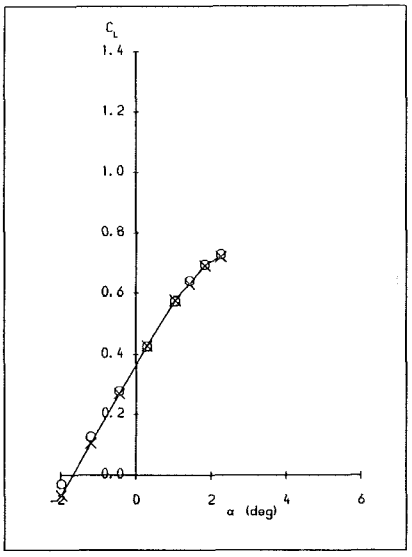

(b) lift vs incidence

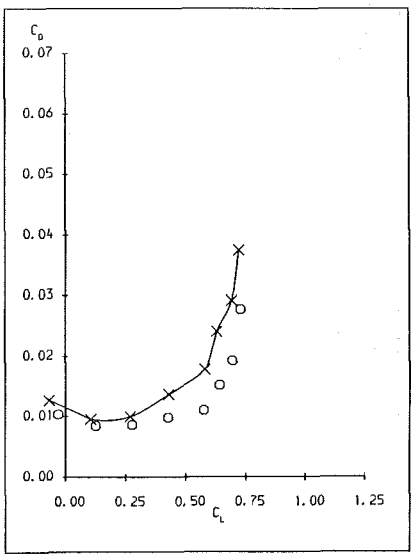

(c) drag vs lift

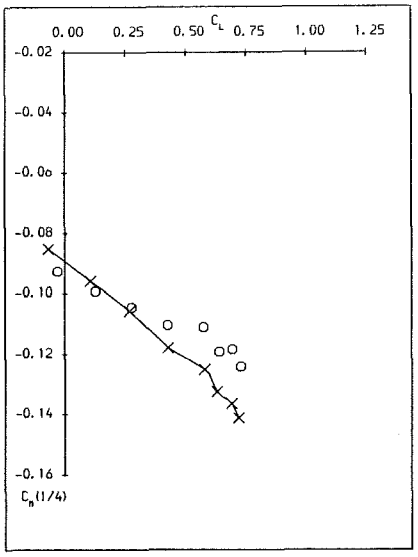

(d) pitching moment vs lift

Fig. 9 Boeing BAC I - M = 0.80 , R = 7.7 x 10^6
o,△ experiment; ——, —×— computation